Li, Z., Qu, W., Young, K. and Qin, Z. (2011) *Earthquake source parameters of the 2009 Mw 7.8 Fiordland (New Zealand) earthquake from L-band InSAR observations.* Earthquake Science, 24 (2). pp. 199-206. ISSN 1674-4519

http://eprints.gla.ac.uk/53843/

Deposited on: 4 August 2011

Earthquake source parameters of the 2009 Mw 7.8 Fiordland (New Zealand) earthquake from L-band Interferometric SAR observations

Zhenhong LI[1,*] Wei QU[2,1], Kateline Young[1] and Qin ZHANG[2]

[1]School of Geographical and Earth Sciences, University of Glasgow, Glasgow G12 8QQ, UK

[2]College of Geology Engineering and Geomatics, Chang'an Uiversity, Xi'an 710054, China

Abstract   The 2009 Mw 7.8 Fiordland (New Zealand) earthquake is the largest to have occurred in New Zealand since the 1931 Mw 7.8 Hawke's Bay earthquake, 1000km to the northwest. In this paper two tracks of ALOS PALSAR interferograms (one ascending and one descending) are used to determine fault geometry and slip distribution of this large earthquake. Modeling the event as dislocation in an elastic half-space suggests that the earthquake resulted from slip on a SSW-NNE orientated thrust fault that is associated with the subduction between the Pacific and Australian plates, with oblique displacement of up to 6.3m. This finding is consistent with the preliminary studies undertaken by the USGS using seismic data.

Key words: Interferometric SAR; New Zealand; earthquake source parameters; Uniform slip modeling; Distributed slip modeling
CLC number：P315.3   **Document code**：A

1 Introduction

On July 15th 2009 (09:22 UTC), a Mw 7.8 earthquake occurred in a region known as Fiordland, which lies along the boundary of the Pacific and Indian-Australian plates (Figure 1), and is a complex area of transition of plate boundary style from Puysegur subduction to Alpine Fault strike slip motion (Davey and Smith, 1983). Christoffel and Van der Linden (1972) account for this complex plate motion using a 'ploughshare' model, in which the Indian plate is dipping obliquely northwards and subducting in a clockwise 'rolling' motion under the Pacific plate at Puysegur Trench.

During the last 20Myr the plate motion has been largely transcurrent, with compressional motion becoming an increasing factor, with highly oblique compression between the two plates in the Fiordland region during the last 15 Myr (Davey and Smith, 1983). Most geophysical features of the Fiordland region can be attributed to this recent subduction event at the Fiordland margin. However, the intermediate depth seismicity appears to arise from a fragment of the Indian plate subducted at Puysegur Trench, and subsequently moved northwards by the transcurrent motion between the two plates. The deformed Indian plate beneath Fiordland is highly active both along its boundary with the Pacific plate and internal to the Indian subducted plate. Over the past two decades, several large earthquakes have occurred in Fiordland, predominantly in a cluster to the northeast of this earthquake. The most recent of these previous large events occurred in August 2003 when a magnitude 7.2 earthquake approximately 100 km to the northwest caused minor damage in Otago and Southland, and numerous landslides across the Fiordland region. The earthquake that occurred on July 15th 2009 was an example of this intermediate depth seismicity, as a result of slip on the subduction thrust interface between the Pacific and Indian plates, the Alpine Fault (Scholz et al, 1973).

Initial fault plane solutions published by the Global Centroid Moment Tensor Project (GCMT, www.globalcmt.org) for the main shock and aftershocks are consistent with predominantly thrust-faulting mechanisms striking SSW- NNE, with significant right-lateral displacements (Table 1). In this study, L-band SAR interferometry was employed to constrain the earthquake source parameters and slip distributions to gain an understanding of the fault mechanism.

Table 1 Source parameters from various source models

Fault segment	Strike (deg)	Dip (deg)	Rake (deg)	Latitude (deg)	Longitude (deg)	Length (km)	Slip (m)	Centroid (km)	Bottom (km)	Moment Magnitude (Mw)
GCMT	25.0 154	26 73	138 70	-45.85	166.26			23.5		7.8
USGS	27 166	33 64	126 69	-45.750	166.577			19		7.8
InSAR	27*	30.5±0.7	144.0±1.6	-45.876±0.6km	166.203±0.5km	57.8±1.4	2.91±0.05	20±0.4	26.8±0.3	7.72

Note: (a) The parameter denoted by "*" is fixed to that derived from USGS. (b) Formal 1σ errors of model fault parameters determined using a Monte Carlo method [*Wright et al.*, 2003]. See Figure 3 for full uncertainties and trade-offs.

The earthquake, in spite of a large magnitude, caused little damage due to its distance from population centres. The ground movement was felt throughout South Island and in North Island. The rupture plane did reach the surface, and a small tsunami was triggered by the event (http://www.natureandco.com, accessed on 15 September 2010).
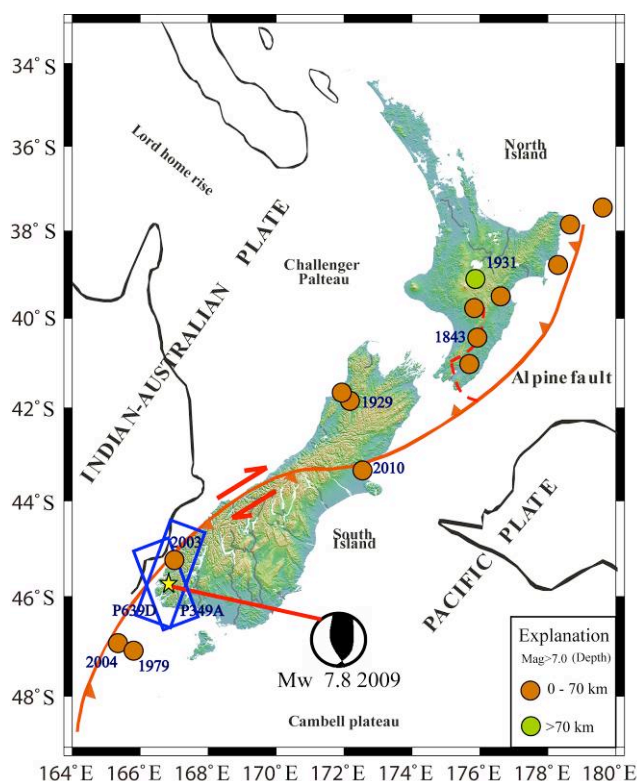
Figure 1 – The Indian-Pacific plate boundary (shaded orange) through New Zealand. Fiordland lies at the southwest end of South Island. The red arrows represent the motion of each tectonic plate relative to the adjacent plate. In the vicinity of the earthquake the Indian plate and Pacific plate are converging at about 35-45mm/yr (USGS) along the Puysegur Trench, with the Indian Plate thrusting under the Pacific plate as shown. The yellow star shows the epicentre of the July 15th 2009 earthquake, with the blue rectangle representing the coverages of two different paths: ascending path 349 (P349A) and descending path 639 (P639D).

2 Interferometric processing

Interferometric SAR (InSAR) can be used to map changes in the Earth's surface from space, utilizing the phase differences in complex (magnitude and phase) Synthetic Aperture Radar (SAR) images acquired in similar geometric conditions, but at two different epochs (e.g. Massonnet and Feigl, 1998). This can be done with sub-centimetre precision and tens-of metres horizontal spatial resolution over large regions (e.g. 100 km × 100 km).

Table 2 shows the SAR data used in this paper: one descending and one ascending tracks from the JAXA Advanced Land Observing Satellite (ALOS). Both pairs of ALOS PALSAR images were processed for both interferograms using the JPL/Caltech ROI_PAC software (version 3.1b) (Rosen et al., 2004). The topographic phase contribution was removed using a 3-arc-sec (~90-m) digital elevation model from the Shuttle Radar Topography Mission (SRTM) (Farr et al, 2007) and the interferograms were unwrapped using the SNAPHU algorithm (Chen and Zebker, 2000) to obtain displacements in the satellite line-of-sight (LOS).

In the rugged terrain and heavy vegetation of the Fiordland region, coseismic deformation signals cannot be resolved by the C-band interferograms (now shown); the ascending interferogram (P349A) spans a time interval between 22 February 2007 and 15 July 2009, approximately two and half years, and the descending interferogram (P639D) spans from 20 July 2008 to 23 July 2009, almost 1 year. Coherence in both interferograms is generally good and deformation is well resolved. This highlights the main advantage of L-band over C-band, i.e. less temporal decorrelation due to its capability to penetrate more deeply in vegetation (e.g. Konca et al, 2008; Li et al., 2009). The shallower 38.7° incidence of PALSAR also helps in the high-relief areas. P639 shows greater coherency with clearer more defined fringes. This may be due to the shorter time span between satellite passes. Both P349A and P639D show that deformation is centred offshore, with defined fringes close to this centre, becoming degraded further away from this centre.

Table 2. ALOS SAR images used in this study

|	Track	Frame	Date 1	Orbit 1	Date2	Orbit 2	Baseline, m
Ascending	349	6240	22 February 2007	05753 (ALOS)	15 July 2009	18502 (ALOS)	845
Descending	639	4540	20 July 2008	13257 (ALOS)	23 July 2009	18625 (ALOS)	454

3 Determining fault parameters using InSAR

To expedite the modelling process, interferograms were downsampled to create more manageable datasets with a modified quadtree decomposition algorithm (Jonsson et al, 2002), a technique which concentrates sampling in areas of high gradients in the LOS displacements. For each interferogram, this reduced the number of datapoints to be modeled from tens of thousands to ~1000 to determine the source mechanism of the 2009 Fiordland earthquake.

Interferometric phase measurements in the satellite line of sight were modelled with uniform slip on a simplified rectangular fault using an elastic half-space dislocation model (Okada, 1985, 1992). An elastic shear modulus of 3.23×10^{10} Pa and a Poisson ratio of 0.25 were used. The strike angle of the fault was fixed to 27º that was given by the United States Geological Society (USGS); this measure was necessary due to lack of data for the west side of the fault. If the strike was not fixed, there would be strong tradeoffs between model parameters, e.g. between strike and location (mainly easting), between strike and slip, between strike and width. Fault parameters (including dip, slip, length, and bottom depth) were then determined by minimizing the squared misfits between the observed and the predicted displacements using a novel hybrid minimization algorithm (Feng and Li, 2010) that combines Particle Swarm Optimization (PSO) (Eberhart and Kennedy,1995) and the downhill simplex algorithm (DSA) (Nelder and Mead, 1965): (1) PSO is employed to perform a global search to find several most optimal local minima; (2) based on the PSO-derived local minima, DSA is then used to determine the global minimum. It is demonstrated in Feng and Li (2010) that the hybrid algorithm has the ability to determine efficiently the global minimum in a nonlinear search space.

Table 1 shows the optimal geometry determined with InSAR observations, suggesting the fault dips 30.5° to the southeast with a uniform slip of 2.9m. To determine parameter errors for the non-linear PSO/simplex integrated

inversion, a Monte Carlo simulation of correlated noise was used (Funning et al, 2005; Parsons et al, 2006; Wright et al, 2003). Figure 3 shows the parameter errors and tradeoffs. Several strong trade-offs between different model parameters are observed: such as between the slip and the rake, between the moment and the x coordinate (i.e. the longitude of the centre), and between the moment and the length.

Figure 2 shows interferograms simulated from the optimal uniform model and their comparisons against with InSAR observations. It is clear that the uniform model is well consistent with InSAR displacements and produces a first order fit to the observed deformation pattern with a small root mean square (RMS) misfit to the data: 9.2cm to the ascending P349A, and 9.0cm to the descending P639D interferograms.
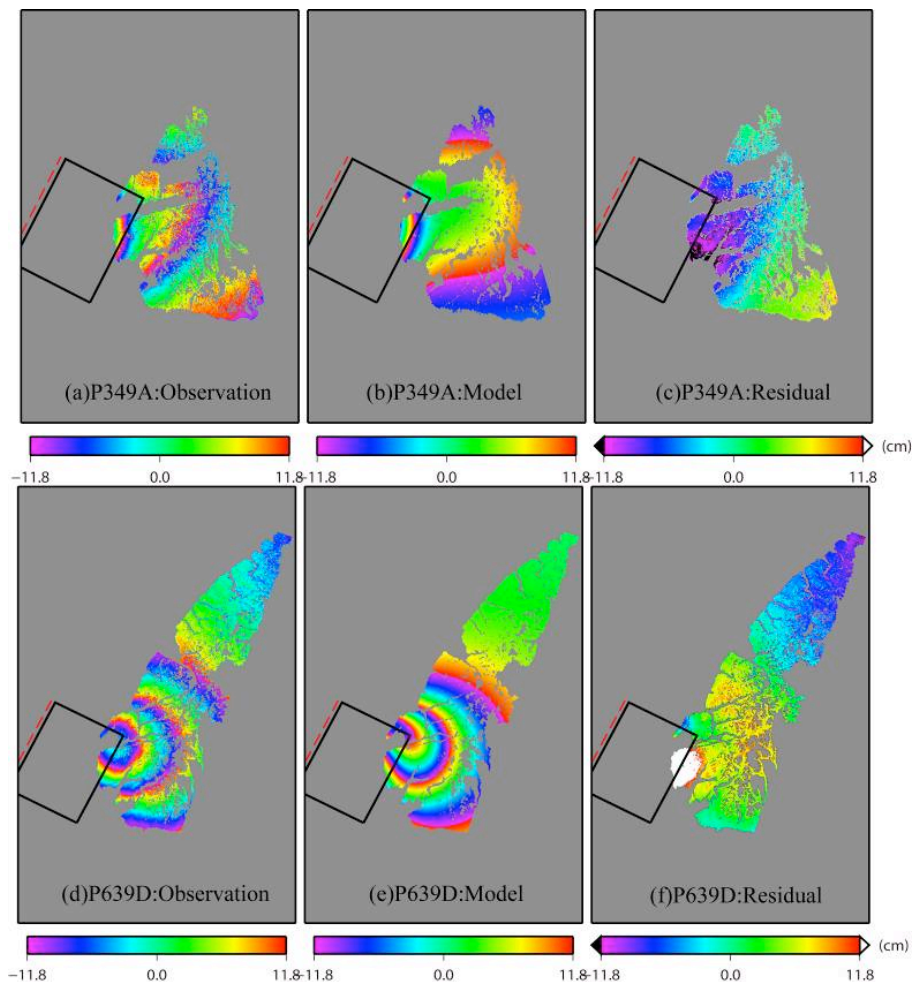
Figure 2 Observed, uniform model, and residual interferograms. (a) P349A interferogram (wrapped): 20070222–20090715. (b) P349A uniform model (wrapped). (c) P349A residual interferogram. (d) P639D interferogram (wrapped): 20080720–20090723. (e) P639D uniform model (wrapped). (f) P639D residual interferogram. Note: (1) The observed and model interferograms are wrapped so that each color cycle from violet to red to violet represents an increase of 23.6 cm in the range to satellite, while the residual one is not wrapped due to its relatively small magnitude. (2) Black rectangles show the map view projections of the fault plane, and dashed red lines indicate the fault rupture projected on the surface that would be expected in the black rectangles if the fault broke the surface.
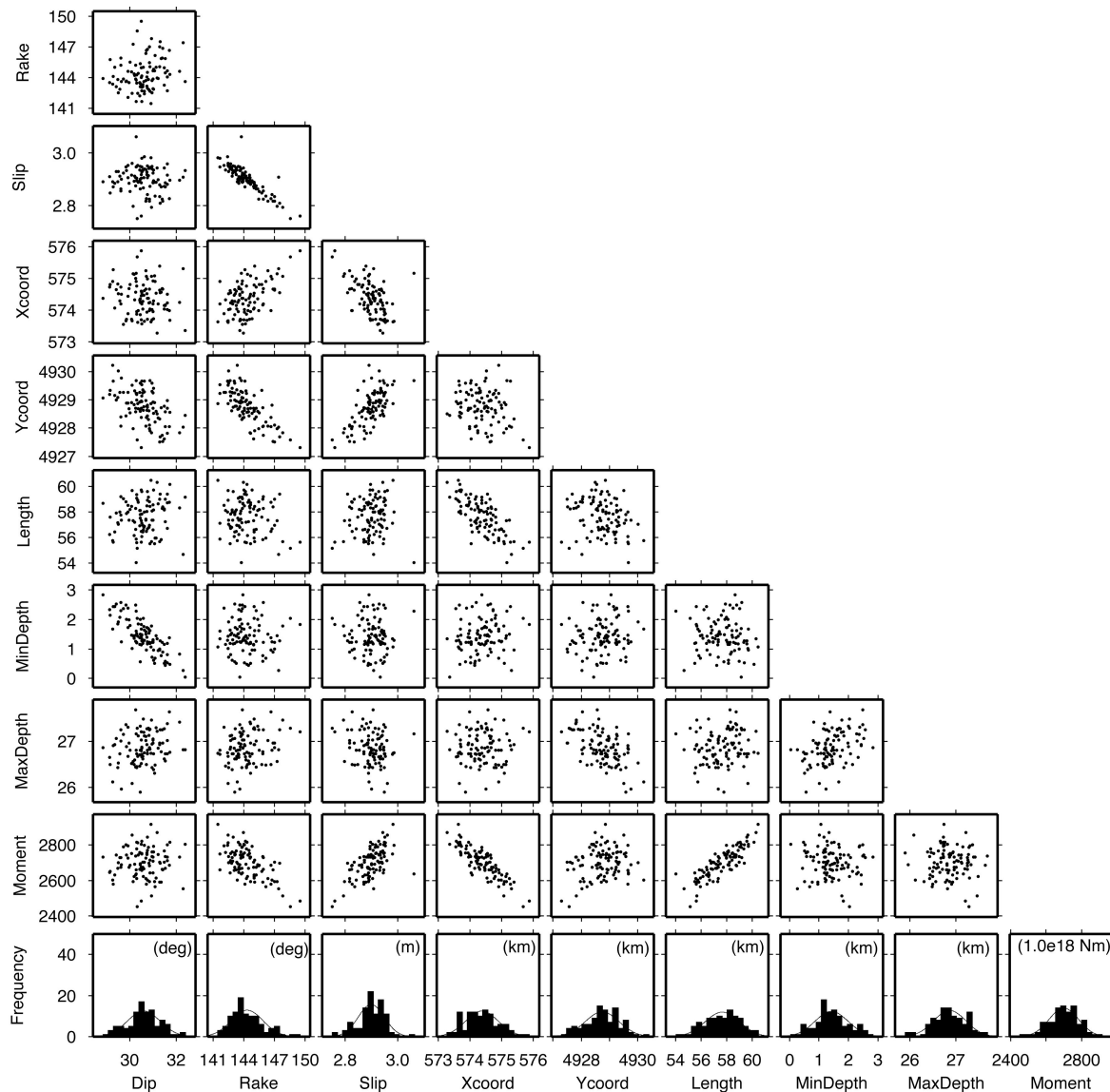
Figure 3 Model parameter trade-offs for uniform-slip model. Each of the 100 dots in each of the upper plots is the best-fit solution for one data set to which Monte Carlo, correlated noise has been added (see text). Histograms summarize the results for each parameter.

4 Distributed slip modelling

Once the orientation of the fault plane has been determined, the model can be further refined by solving for the distribution of slip on the fault. Assuming the fault geometry for a NNE-SSW fault plane determined in the uniform slip modeling, we extended the fault plane along strike and downdip by increasing its total length to 120 km and down dip width to 60km, and then divided the fault into 120 by 60 subfaults each measuring 4 km by 4 km. The best fitting values of strike-slip and dip-slip motion for each subfault were solved in a least squares sense while Laplacian smoothing and a nonnegative least squares algorithm were employed to prevent unphysical oscillatory slip (e.g., Harris and Segall, 1987; Segall and Harris, 1987; Bro and Jong, 1997; Vasco, 1998; Wright et al, 2003; Funning et al, 2005; Li et al., 2008).

Figure 4 shows the results of the distributed slip modelling. Slip is concentrated within the upper 20 km (equivalent to c. 40km along dip) of the fault, peaking at 6.3 m at a depth of 0-2km. To determine the level of uncertainty in the slip estimates, the slip inversion was applied to the 100 perturbed data sets generated using realistic correlated noise as for the uniform models. The standard deviation of the slip on each subfault gives a measure of the error on each slip estimate. It is clear that the slips in Figure 4(a) are generally one order of magnitude greater than their corresponding errors (Figure 4(b)), indicating the reliability of the slip distribution. From Figure 4 we can easily find that the predominant fault movement is thrust with significant right lateral slip in the epicentre. This fits with the tectonic environment: the relative motion of Australian Plate and Pacific Plate, westward for the Pacific plate, and northward for the Australian plate, resulted in collision and compression of the plate edges, giving rise to the Australian Plate that subducts below the Pacific Plate; hence the Alpine Fault should have the oblique characteristic.

The observed and modelled data were compared and the difference between the two shown as residual displacement, the result of subtracting the model interferogram from the observed interferogram. The results of the comparative analysis show very good agreement between the observed and modelled data, with small RMS misfits: 8.6cm to the ascending P349A, and 7.1cm to the descending P639D interferograms (Figure 5).
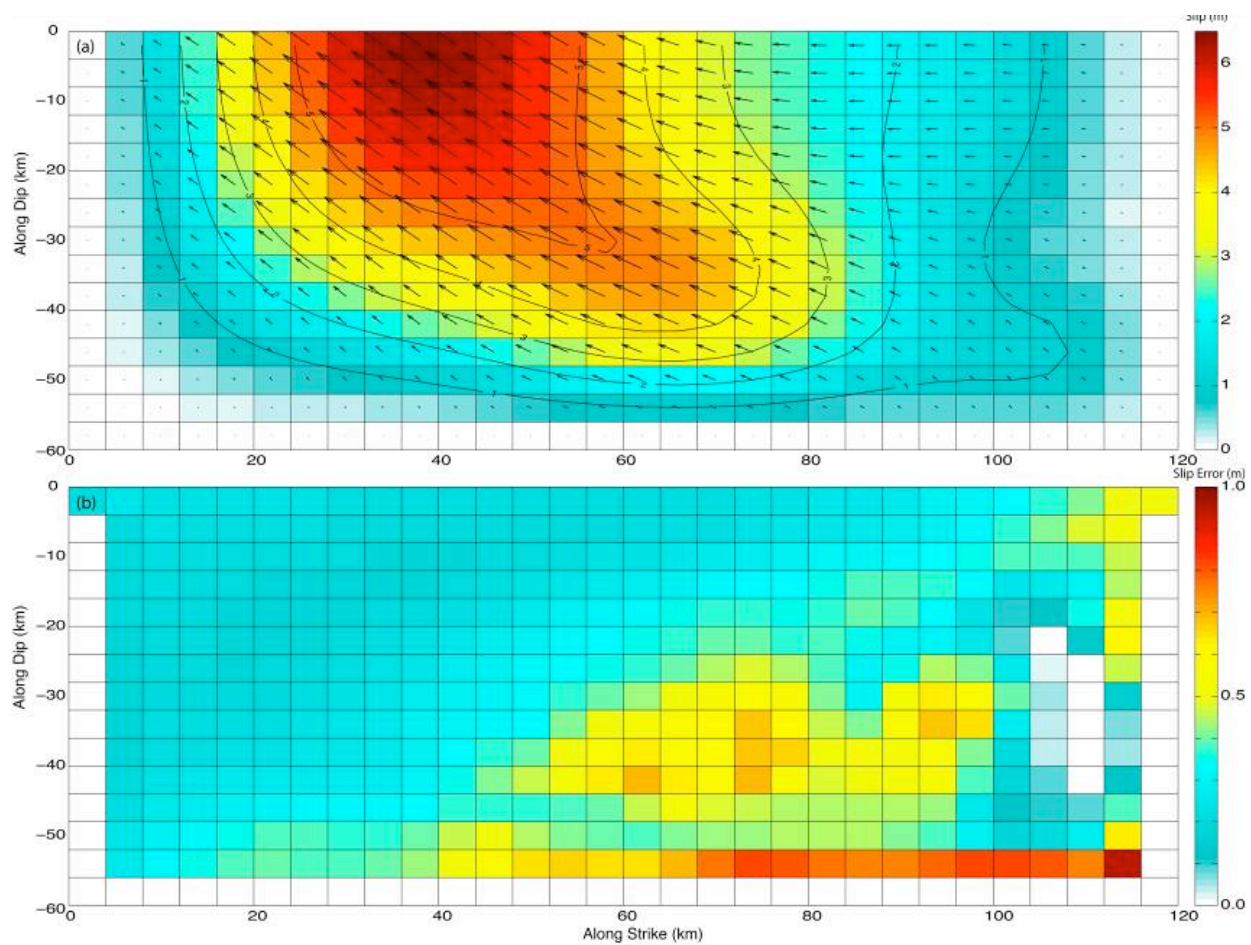
Figure 4 (a) Slip distribution for a fault plane 120 km long, 60 km downdip wide, and dipping 30.50. (b) Uncertainty in fault slip estimated by a Monte Carlo process (e.g. Wright et al., 2003; Funning et al., 2007).
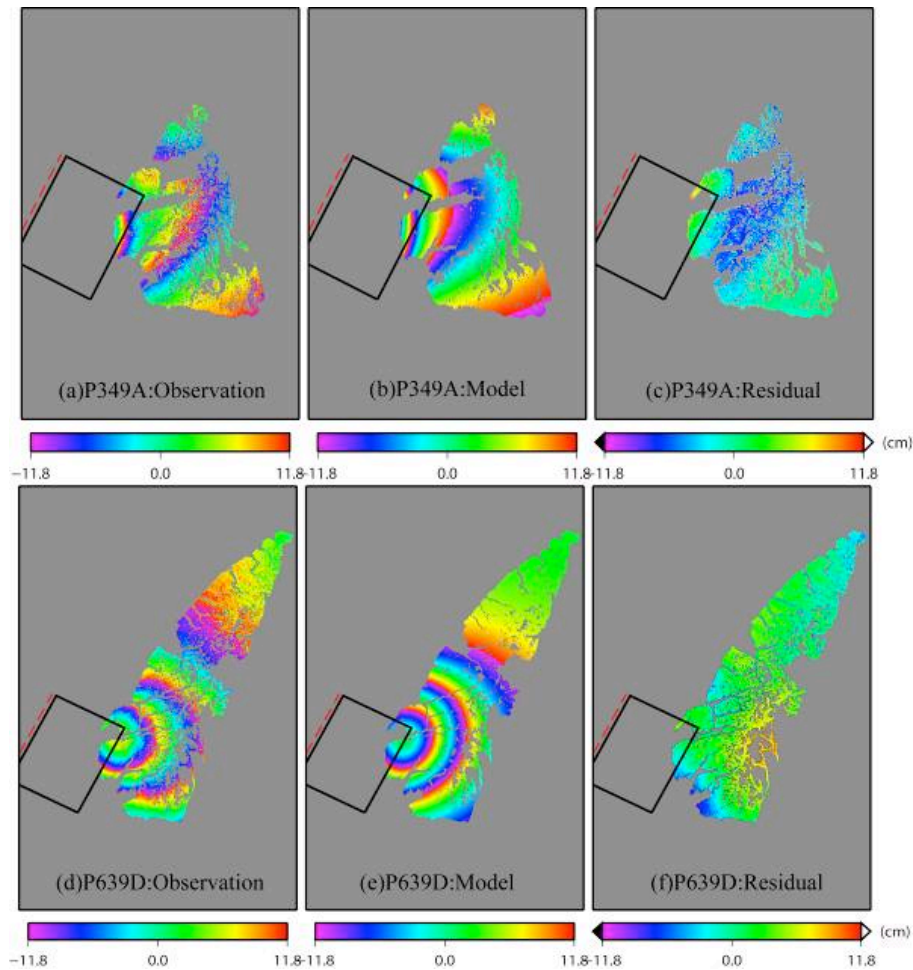
Figure 5 Observed, distributed model, and residual interferograms. (a) P349A interferogram (wrapped): 20070222–20090715. (b) P349A distributed model (wrapped). (c) P349A residual interferogram. (d) P639D interferogram (wrapped): 20080720–20090723. (e) P639D distributed model (wrapped). (f) P639D residual interferogram. Note: (1) The observed and model interferograms are wrapped so that each color cycle from violet to red to violet represents an increase of 23.6 cm in the range to satellite, while the residual one is not wrapped due to its relatively small magnitude. (2) Black rectangles show the map view projections of the fault plane, and dashed red lines indicate the fault rupture projected on the surface that would be expected in the black rectangles if the fault broke the surface.

5 Conclusions

Using JAXA ALOS PLASAR images, two coseismic interferograms were generated for the 2009 Mw 7.8 earthquake, showing that this large event lifted a large area of land around the epicenter up to 1 metre. Inverting the two coseismic interferograms for a uniform slip model suggests this earthquake is associated with a SSW-NNE orientated thrust fault located in the boundary between the Pacific and Australian plates. It is worthy mentioning that there was no measurement for the west side of the fault, which imposed a big challenge on the uniform modelling. To overcome this challenge, the strike angle was set using information given by the United States Geological Society (USGS). A further distributed slip model suggests that the peak slip of 6.3 m is located at a depth of 0–2 km. These findings fit with the tectonic setting described in this paper.

Study in the South and North Islands of New Zealand is essential because of the complex nature of the Australia-Pacific plate boundary and the seismic hazard posed by the active structures. Its high frequency of large events (e.g. 6 earthquakes with Mw > 7.0 since 1990) makes this area as an exceptional natural laboratory for investigating earthquake and fault interactions. Future studies could investigate the recent 2010 Mw 7.0 Christchurch earthquake (see Figure 1) occurred in South Island, New Zealand, 500km to the northeast of the 2009 Mw 7.8 event (http://web2.ges.gla.ac.uk/~zhli/Darfield_EQ.htm and http://comet.nerc.ac.uk/current_research_newz.html), and then assess the stress interactions between these two large events.

References

Bro R., and S D Jong (1997). A fast non-negativity-constrained least squares algorithm. *J. Chemometr.,* **11**(5);393-401.

Bird, P., (2003). An updated digital model of plate boundaries. *Geochem.Geophys. Geosyst.,* **4**(3): 1027-80

Christoffel, D A and Van D L, W J M (1972). Macquarie Ridge-New Zealand Alpine Fault transition, in Antarctic Oceanology II, the Australiaiz-New Zealand sector. *Antarctic Research Series,* **19**, 235-242.

Chen, C. W., and H. A. Zebker (2000). Network approaches to two-dimensional phase unwrapping: intractability and two new algorithms.*Journal of the Optical Society of America A-Optics Image Science and Vision*, **17**, 401-414.

Davey, F J. and Smith, E G C (1983). The tectonic setting of the Fiordland region, south-west New Zealand. *Geophys. J. R. astr. SOC,* **72**:23-38.

Eberhart, R. C., and J. Kennedy (1995). A new optimizer using particle swarm theory. *paper presented at Proceedings of the Sixth International Symposium on Micromachine and Human Science, Nagoya, Japan.*

Funning, G J, B Parsons, T J.Wright, J A Jackson, and E J Fielding (2005). Surface displacements and source parameters of the Bam (Iran) earthquake from Envisat advanced synthetic aperture radar imagery. *J. Geophys. Res.,* **110**, B09406, doi:10.1029/2004JB003338.

Feng, W., and Z. Li (2010). A novel hybrid PSO/simplex algorithm for determining earthquake source parameters using InSAR observations.*Progress in Geophysics,* **25**(4), 1189-1196. (in Chinese with English abstract).

Farr, T. G., et al. (2007). The Shuttle Radar Topography Mission. *Rev. Geophys.,* **45**, RG2004, doi:2010.1029/2005RG000183.

Harris, R A., and P. Segall (1987). Detection of a locked zone at depth on the Parkfield, California, segment of the San Andreas fault. *J. Geophys. Res.,* **92**: 7945 – 7962.

Jónsson, S., H. Zebker, P. Segall, and F. Amelung (2002). Fault slip distribution of the 1999 Mw 7.1 Hectlor Mine earthquake, California, estimated from satellite radar and GPS measurements. *Bulletin of the Seismological Society of America,* **92**(4), 1377-1389.

Konca, A. O., Avouac, J.-P., Sladen, A., Meltzner, A. J., Sieh, K., Fang, P., Li, Z., Galetzka, J., Genrich, J., Chlieh, M., Natawidjaja, D. H., Bock, Y., Fielding, E. J., Ji, C., and Helmberger, D. V.: Partial rupture of a locked patch of the Sumatra megathrust during the 2007 earthquake sequence, *Nature*, 456, 631-635, 2008.

Li Z., Feng W, Xu Z., Cross, P and Zhang J(2008). The 1998 Mw 5.7 Zhangbei-Shangyi (China) earthquake revisited: A buried thrust fault revealed with interferometric synthetic aperture radar. *Geochemistry Geophysics Geosystems,* **9**(4). Q04026, doi:10.1029/2007GC001910

Li, Z, Liu Y, Zhou X, Cross, P. and Feng W (2009). Using small baseline Interferometric SAR to map nonlinear ground motion: a case study in Northern Tibet. *Journal of Applied Geodesy* **3**:163-170.

Massonnet, D, and K L Feigl (1998). Radar interferometry and its application to changes in the Earth's surface. *Rev. Geophys.,* **36**: 441–500.

Nelder, J. A., and R. Mead (1965). A simplex method for function minimization. *the Computer Journal,* **7**(4), 308-313.

Okada, Y(1985). Surface deformation due to shear and tensile faults in a half-space. *Bulletin of the Seismological Society of America,* **75**(4):1135-1154.

Okada, Y. (1992). Internal deformation due to shear and tensile faults in a half-space. *Bulletin of the Seismological Society of America,* **82**(2), 1018-1040.

Parsons, B., T. Wright, P. Rowe, J. Andrews, J. Jackson, R. Walker, M. Khatib, M. Talebian, E. Bergman, and E. R. Engdahl (2006), The 1994 Sefidabeh (eastern Iran) earthquakes revisited: new evidence from satellite radar interferometry and carbonate dating about the growth of an active fold above a blind thrust fault, *Geophysical Journal International*, 164(1), 202-217, doi: 210.1111/j.1365-1246X.2005.02655.x.

Rosen, P . A., S. Hensley, G. Peltzer, and M. Simons(2004). Updated Repeat Orbit Interferometry package released. *EOS, TRANSACTIONS, American Geophysical Union*, **85**(5),47

Segall, P, and R A Harris (1987). The earthquake deformation cycle on the San Andreas fault near Parkfield, California. *J. Geophys. Res.,* **92**(10):511–525

Scholz, C H., Rynn, J M W., Weed, R W. and Frohlich, C(1973). Detailed Seismicity of the Alpine Fault Zone and Fiordland Region, New Zealand. *Geologiacl Society of America Bulletin*, **84**(10):3297-3316.

Vasco, D W(1998). Regularization and trade-off associated with nonlinear geophysical inverse problems: penalty homotopies. *Inverse Problems*,**14:** 1033-1052.

Wessel, P., and W. H. F. Smith (1998), New, improved version of the Generic Mapping Tools released, *EOS Trans. AGU*, 79, 579.

Wright, T J, Z Lu, and C Wicks (2003). Source model for the Mw 6.7, 23 October 2002, Nenana Mountain Earthquake (Alaska) from InSAR. *Geophys. Res. Lett.,* **30**(18),

1974.